

Supplementary Material for: A Novel Rule-Based Algorithm for Assigning Myocardial Fiber Orientation to Computational Heart Models

J.D. Bayer,¹ R.C. Blake,¹ G. Plank,² N.A. Trayanova¹

¹ Department of Biomedical Engineering and Institute for Computational Medicine at The Johns Hopkins University, Baltimore, MD, USA

² Institute of Biophysics and Center for Physiological Medicine at the Medical University of Graz, Graz, Austria

Correspondence: Jason D. Bayer

Address: 218 Hackerman Hall
3400 N Charles Street
Baltimore, MD 21218

Tel: 410-516-4375

Fax: 410-516-5294

email: jbayer5@jhmi.edu

1 LDRB Algorithm and Functions

Algorithm DefineFibers ($\Omega, \alpha_s(\cdot), \beta_s(\cdot), \alpha_w(\cdot), \beta_w(\cdot)$)

Input: Ω - a conformal mesh

Input: $\alpha_s, \beta_s : [0, 1] \rightarrow \theta$ - functions for fiber and sheet angle within the septum, respectively, from left (=0) to right (=1) ventricle surfaces

Input: $\alpha_w, \beta_w : [0, 1] \rightarrow \theta$ - functions for fiber and sheet angle within the wall respectively, from the endocardial surface (=0) to epicardial surface (=1)

Require: $\alpha_w(0) = \alpha_s(0) = \alpha_s(1) \bmod \pi$

Require: $\beta_w(0) = \beta_s(0) = \beta_s(1) \bmod \pi$

1 Define surfaces $\partial\Omega_{epi}, \partial\Omega_{lv}, \partial\Omega_{rv}$

2 $\phi_{epi} = \text{Laplace}(\Omega, \partial\Omega_{epi}, \partial\Omega_{lv} \cup \partial\Omega_{rv})$

3 $\phi_{lv} = \text{Laplace}(\Omega, \partial\Omega_{lv}, \partial\Omega_{epi} \cup \partial\Omega_{rv})$

4 $\phi_{rv} = \text{Laplace}(\Omega, \partial\Omega_{rv}, \partial\Omega_{epi} \cup \partial\Omega_{lv})$

5 Define surfaces $\partial\Omega_{base}, \partial\Omega_{apex}$

6 $\Psi_{ab} = \text{Laplace}(\Omega, \partial\Omega_{base}, \partial\Omega_{apex})$

7 **for** each point x in the mesh **do**

8 $Q_{lv} = \text{orient} \left(\text{axis}(\nabla\Psi_{ab}, -\nabla\phi_{lv}), \alpha_s \left(\frac{\phi_{rv}}{\phi_{lv} + \phi_{rv}} \right), \beta_s \left(\frac{\phi_{rv}}{\phi_{lv} + \phi_{rv}} \right) \right)$

9 $Q_{rv} = \text{orient} \left(\text{axis}(\nabla\Psi_{ab}, \nabla\phi_{rv}), \alpha_s \left(\frac{\phi_{rv}}{\phi_{lv} + \phi_{rv}} \right), \beta_s \left(\frac{\phi_{rv}}{\phi_{lv} + \phi_{rv}} \right) \right)$

10 $Q_{endo} = \text{bislerp} \left(Q_{lv}, Q_{rv}, \frac{\phi_{rv}}{\phi_{lv} + \phi_{rv}} \right)$

11 $Q_{epi} = \text{orient} (\text{axis}(\nabla\Psi_{ab}, \nabla\phi_{epi}), \alpha_w(\phi_{epi}), \beta_w(\phi_{epi}))$

12 $(F \ S \ T) = \text{bislerp}(Q_{endo}, Q_{epi}, \phi_{epi})$

13 Define F as the longitudinal axis, S as the sheet normal axis, and T as the transverse axis of fiber orientation for point x

14 **end for**

Function 1: Laplace($\Omega, \Gamma_1, \Gamma_0$)

Input: Ω - a conformal mesh

Input: Γ_1 - surface locations on Ω where the Laplace function should be 1

Input: Γ_0 - surface locations on Ω where the Laplace function should be 0

1 Find $\partial\Omega$, the surface of mesh Ω

2 Solve the following partial differential equation:

$$\begin{aligned} \nabla^2 \Theta(x) &= 0 \quad \text{in } \Omega \\ \Theta &= 1 \quad \text{on } \Gamma_1 \\ \Theta &= 0 \quad \text{on } \Gamma_0 \\ \nabla \Theta \cdot n &= 0 \quad \text{on } \partial\Omega - \Gamma_1 - \Gamma_0 \end{aligned}$$

3 **return** $\Theta(x)$

Function 2: axis($\nabla\psi, \nabla\phi$)

Input: $\nabla\psi$ - a vector pointing in the apicobasal direction.

Input: $\nabla\phi$ - a vector pointing in the transmural direction.

$$1 \quad \hat{e}_1 = \frac{\nabla\psi}{\|\nabla\psi\|}$$

$$2 \quad \hat{e}_2 = \frac{\nabla\phi - (\hat{e}_0 \cdot \nabla\phi)\hat{e}_0}{\|\nabla\phi - (\hat{e}_0 \cdot \nabla\phi)\hat{e}_0\|}$$

$$3 \quad \hat{e}_0 = \hat{e}_1 \times \hat{e}_2$$

$$4 \quad \text{return } Q = (\hat{e}_0 \quad \hat{e}_1 \quad \hat{e}_2)$$

Function 3: orient(Q, α, β)

Input: Q - 3x3 orthogonal matrix

Input: α, β - fiber and sheet angle, respectively

$$\text{return } Q' = Q \begin{pmatrix} \cos \alpha & -\sin \alpha & 0 \\ \sin \alpha & \cos \alpha & 0 \\ 0 & 0 & 1 \end{pmatrix} \begin{pmatrix} 1 & 0 & 0 \\ 0 & \cos \beta & \sin \beta \\ 0 & -\sin \beta & \cos \beta \end{pmatrix}$$

Function 4: bislerp(Q_A, Q_B, t)

Input: Q_A, Q_B - two 3x3 orthogonal matrices

Input: $t \in [0, 1]$ - interpolation factor, $0 \rightarrow Q_A$ and $1 \rightarrow Q_B$

- 1 $q_A = \text{rot2quat}(Q_A)$
- 2 $q_B = \text{rot2quat}(Q_B)$
- 3 Find $q_M \in \{\pm q_A, \pm i \cdot q_A, \pm j \cdot q_A, \pm k \cdot q_A\}$ that maximizes $\|q_M \cdot q_B\|$
- 4 **return** $Q_{AB} = \text{quat2rot}(\text{slerp}(q_M, q_B, t))$

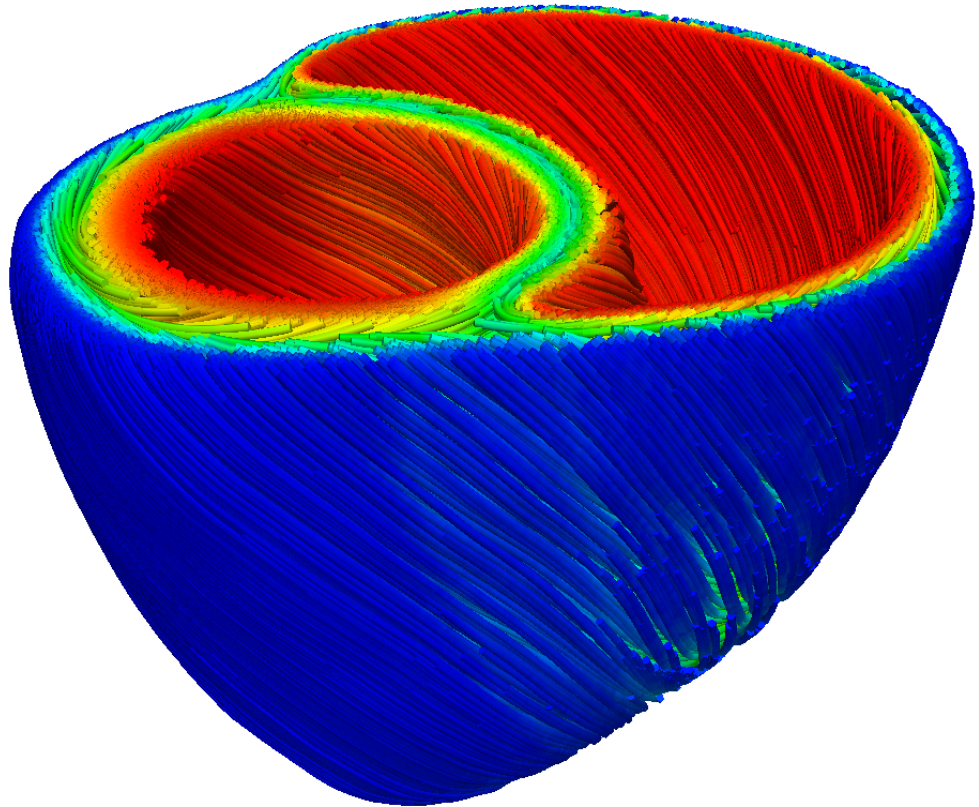
bislerp is used for interpolating the fiber orientation, which is a straight-forward adaptation of quaternion spherical linear interpolation,³ also known as “slerp”, to account for the bidirectional nature of fiber orientation. Quaternions are a generalization of complex numbers, where every right-handed axis system Q_A can be transformed into a unit quaternion q_A and vice versa. One can find the standard algorithms rot2quat and quat2rot for performing this conversion in Function 4 above.³ **slerp** is an algorithm for interpolating unit quaternions, such that every interpolant is also a unit quaternion, and therefore represents an intermediate orthogonal axis system. **slerp** also guarantees that its intermediate axis systems are the “best”, in that they minimize the rotation from Q_A to Q_B and rotate through only one axis.

The standard **slerp** algorithm is very close to what we need in a fiber orientation interpolant, but it does not account for the bidirectional nature of fibers. If we rotate a fiber axis system 180° about any of its primary axes, this should not change the fiber orientation. In the notation of quaternions, $\pm q, \pm i \cdot q, \pm j \cdot q$, and $\pm k \cdot q$ all correspond to the same fiber orientation. When we interpolate two fiber orientations, we want to rotate through the smallest angle possible. We can find which of the

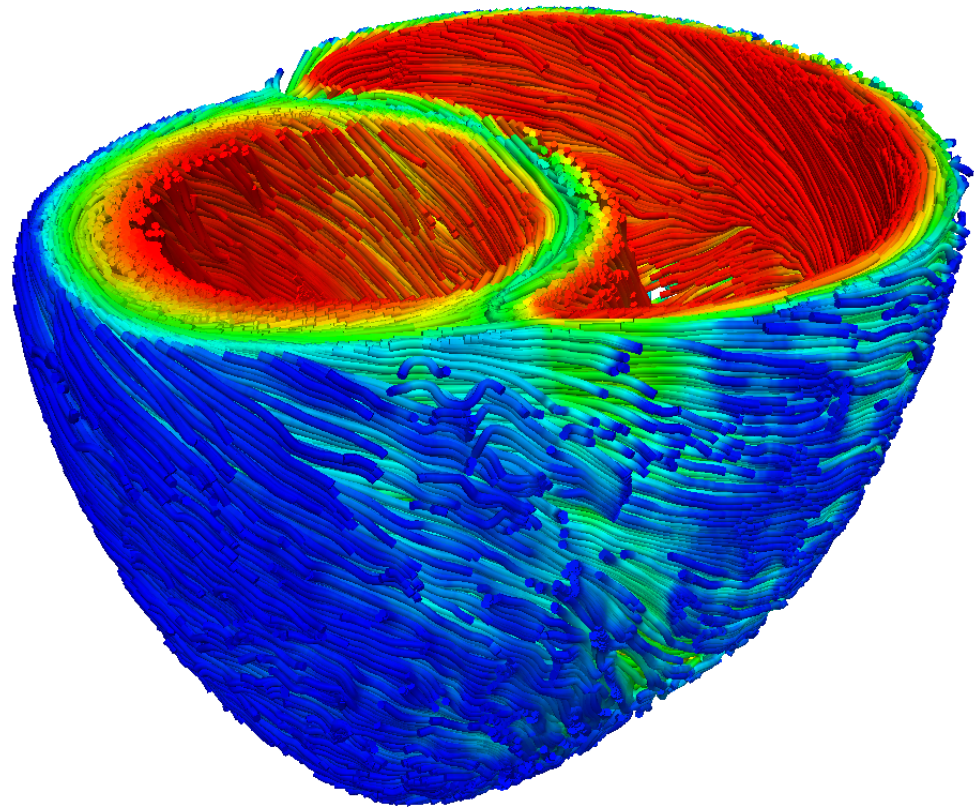
equivalent quaternions are closest by maximizing $\|q_A \cdot q_B\|$, much like we would for a vector dot product. This yields Function 4.

2 High-Resolution Images of Streamlined LDRB Fiber Orientation in the Canine Ventricles

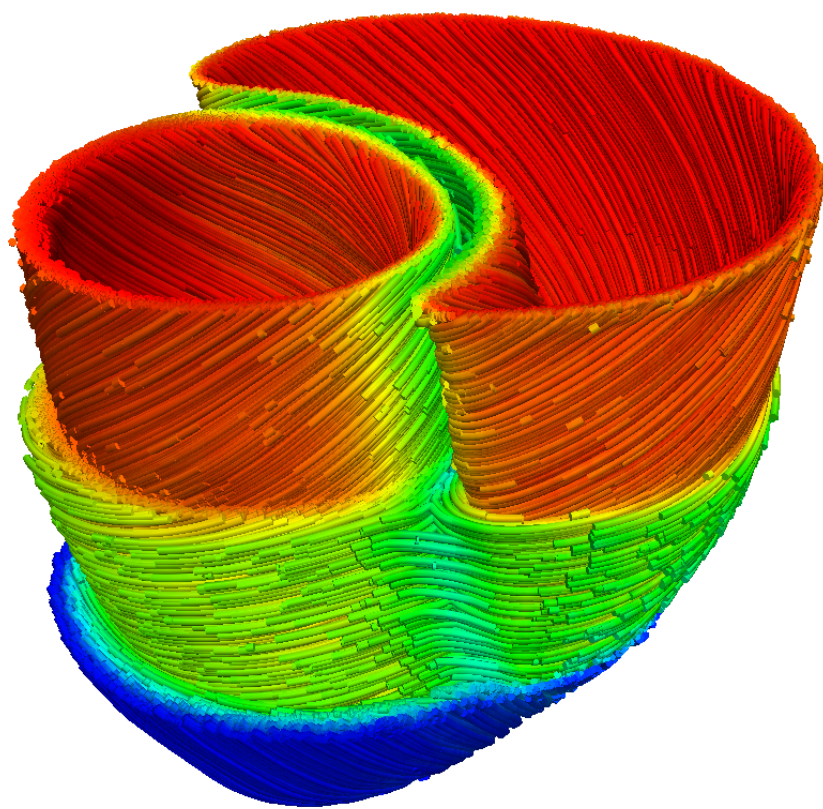
The figures below (S-Figures 1-12) are high-resolution images of the fiber orientation from Figures 3-5.A,B in the manuscript.



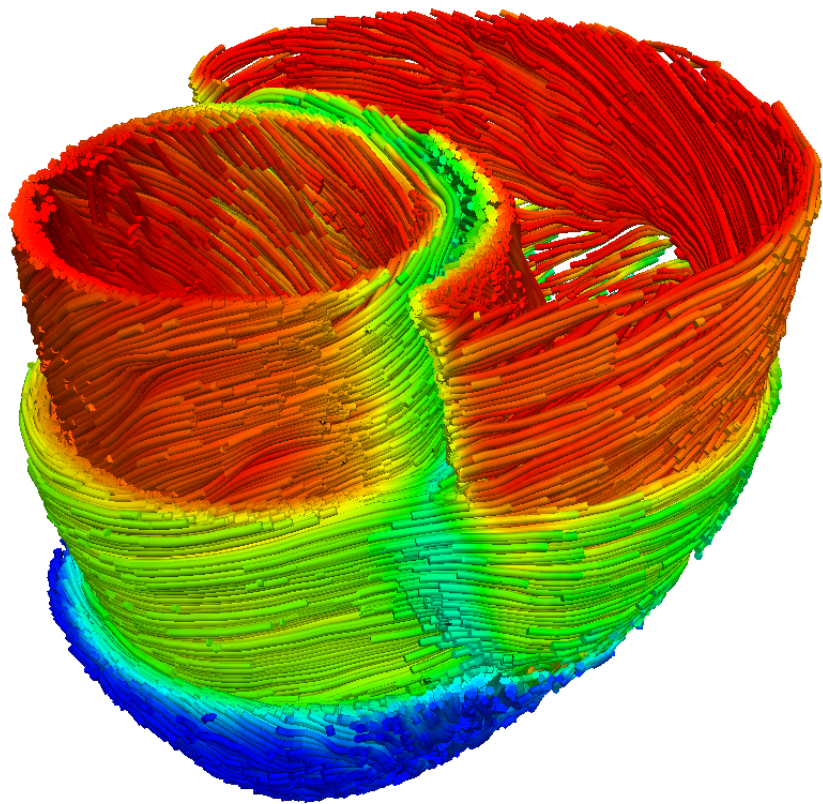
S-Figure 1: Streamlined LDRB F



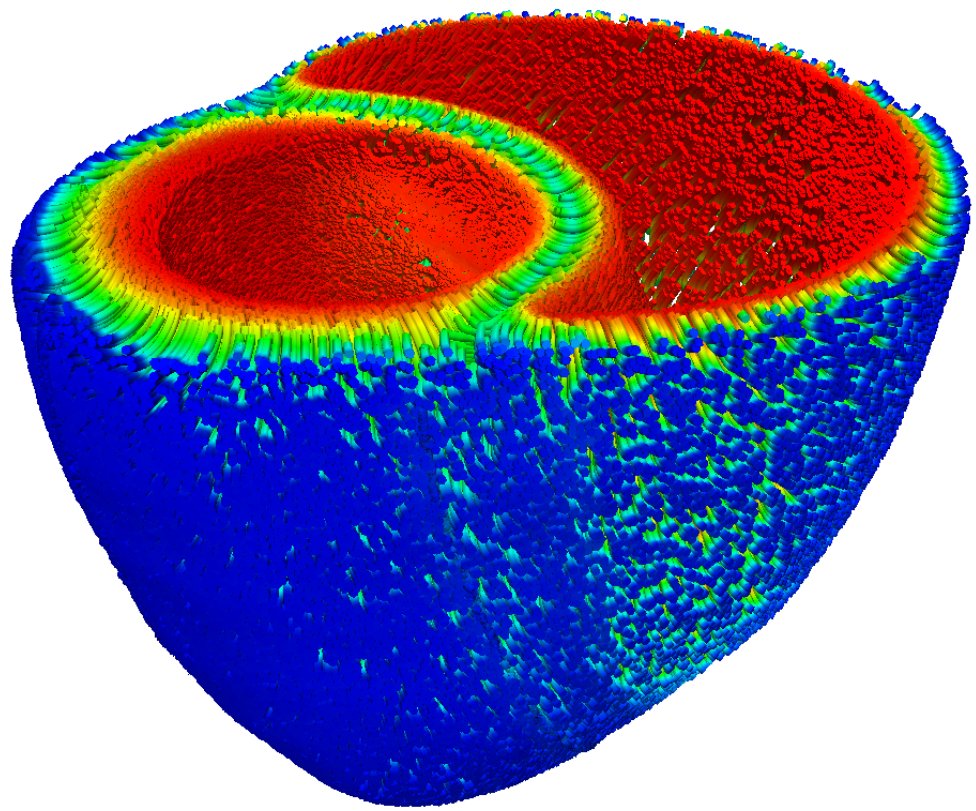
S-Figure 2: Streamlined DTI-derived F



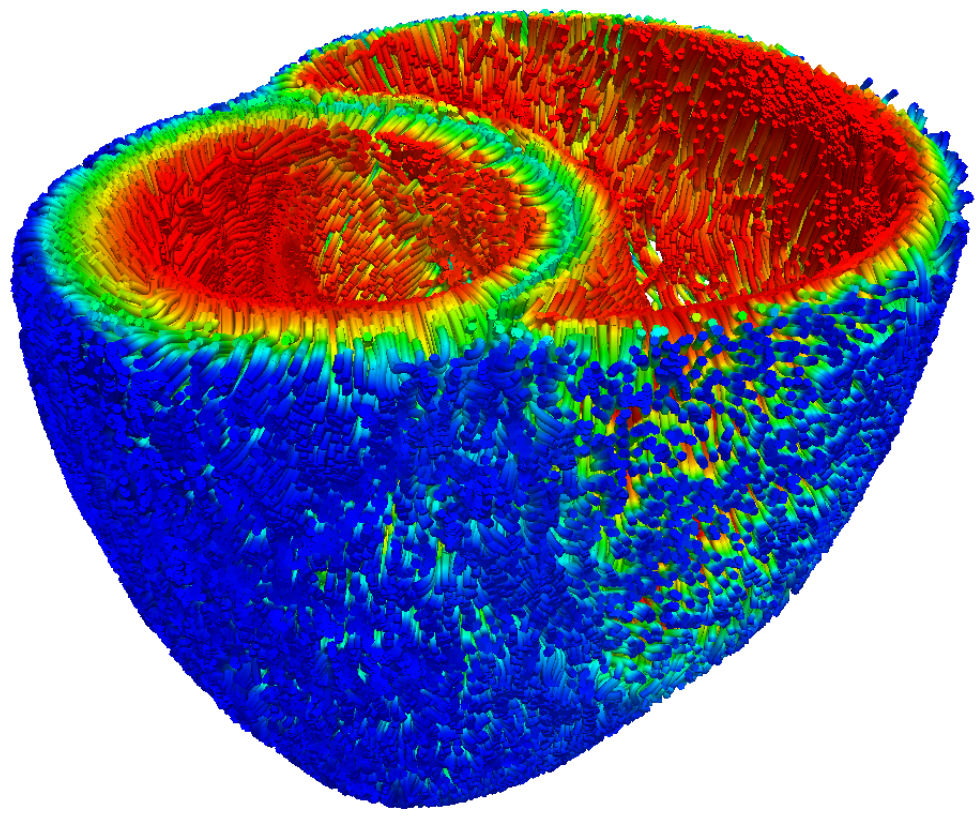
S-Figure 3: Streamlined LDRB F



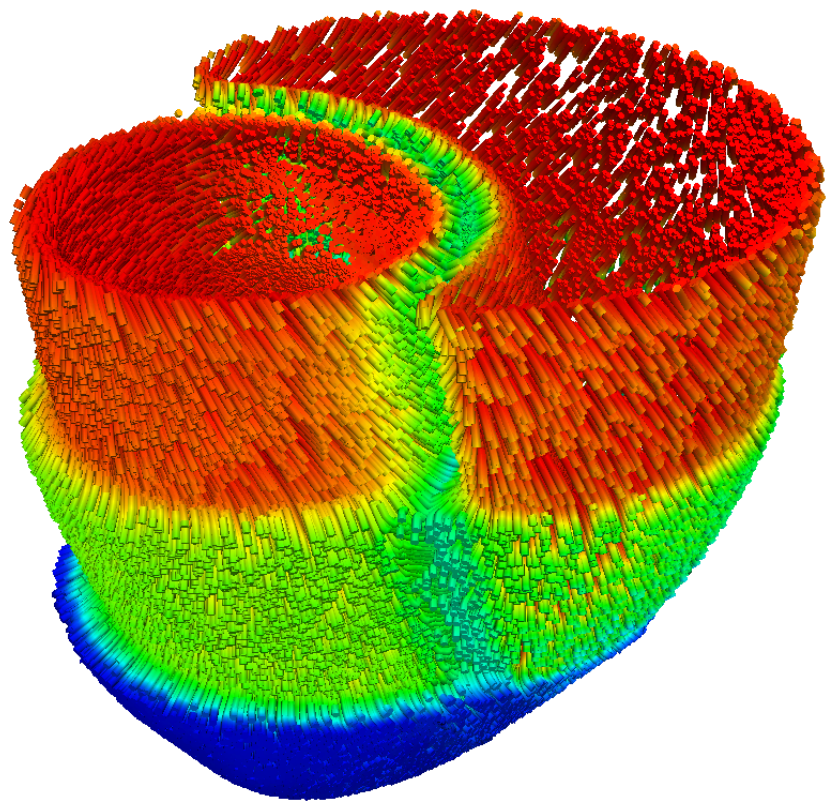
S-Figure 4: Streamlined DTI-derived F



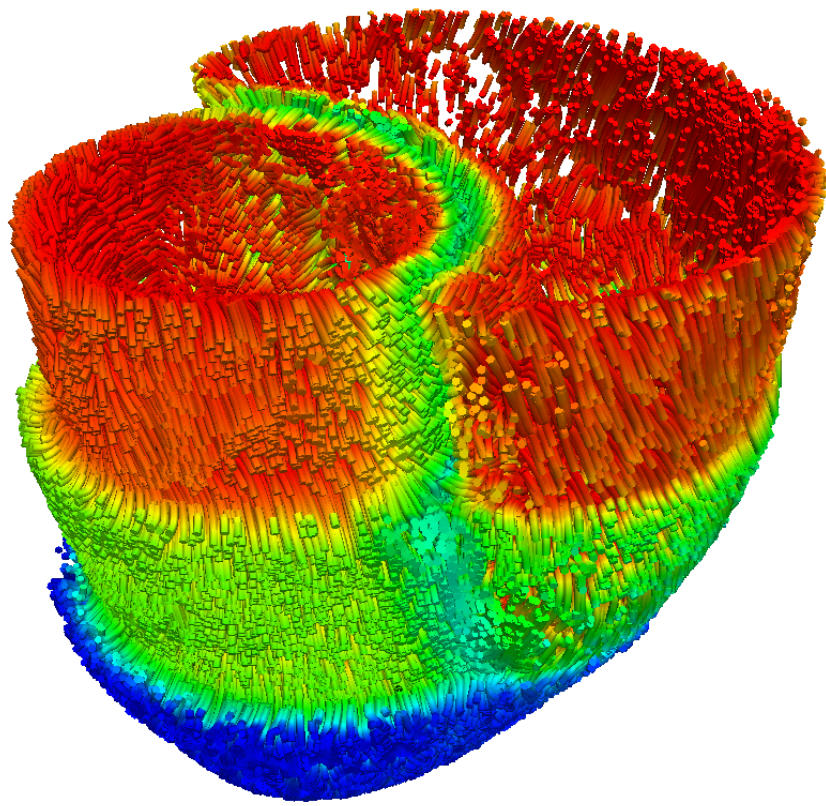
S-Figure 5: Streamlined LDRB T



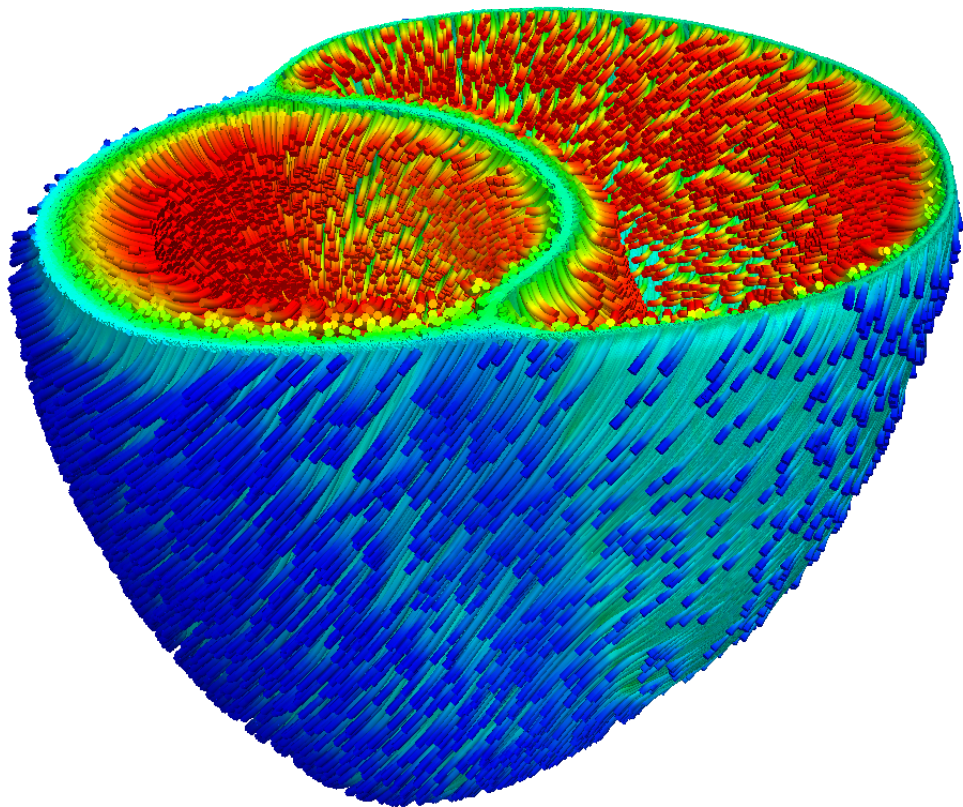
S-Figure 6: Streamlined DTI-derived T



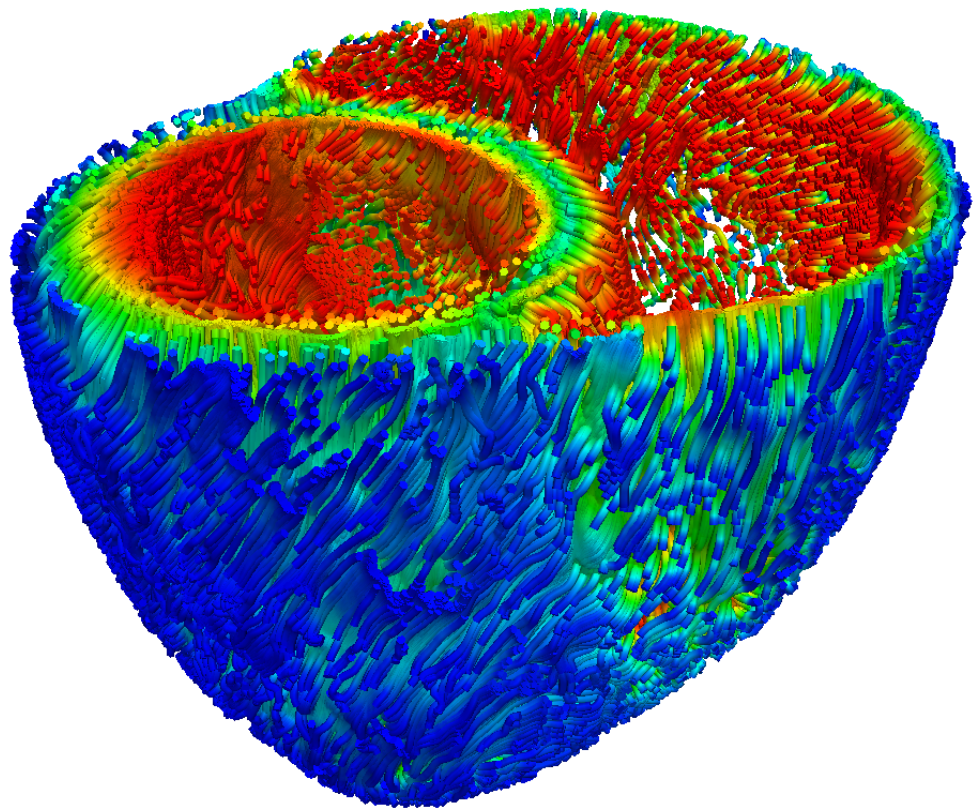
S-Figure 7: Streamlined LDRB T



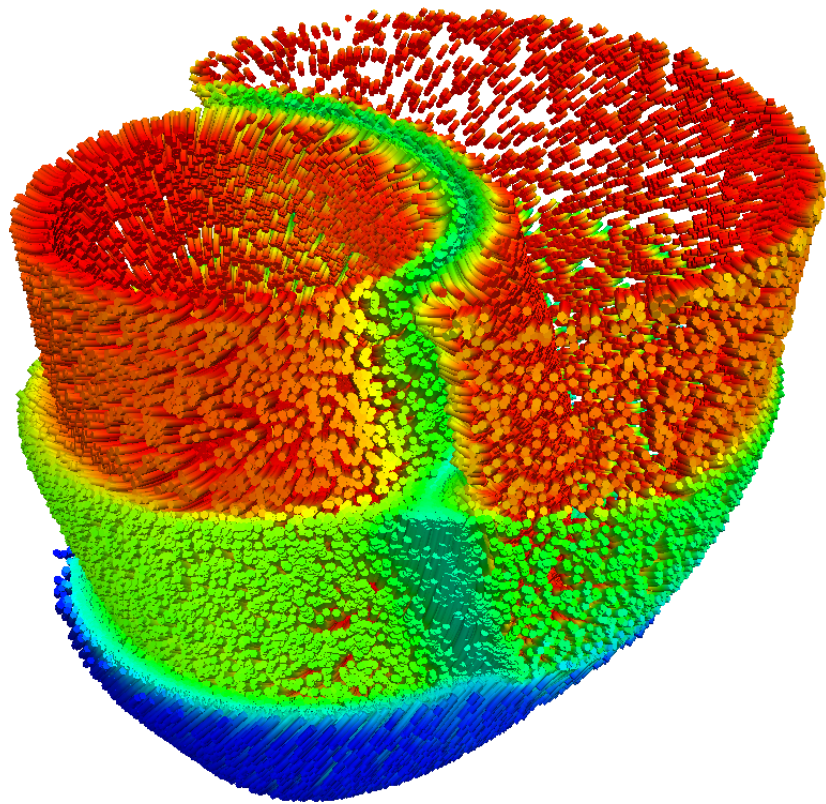
S-Figure 8: Streamlined DTI-derived T



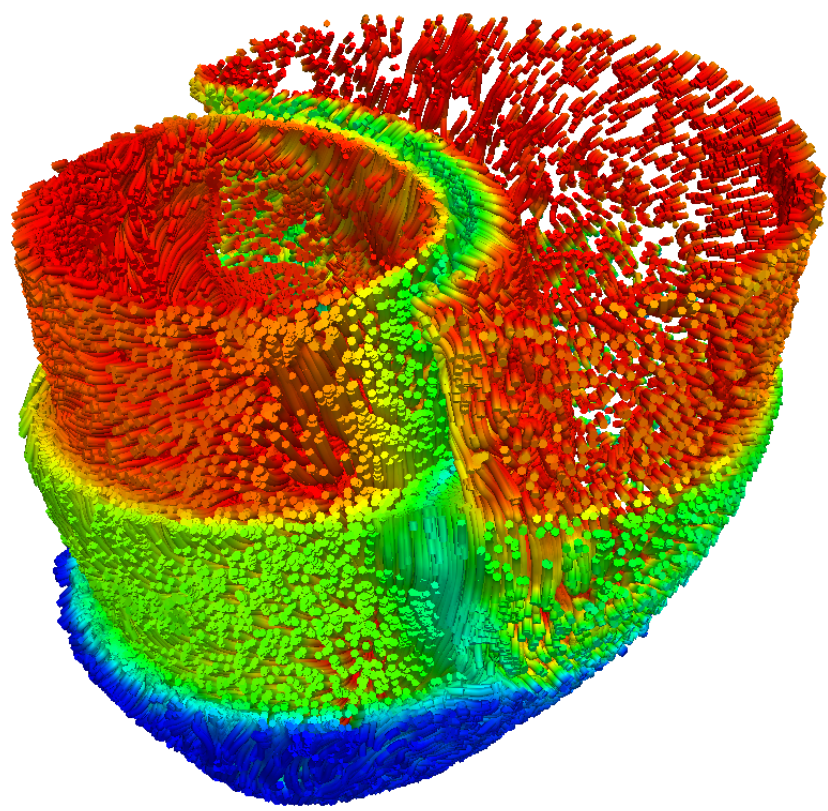
S-Figure 9: Streamlined LDRB S



S-Figure 10: Streamlined DTI-derived S



S-Figure 11: Streamlined LDRB S



S-Figure 12: Streamlined DTI-derived S

3 Comparison of Activation Maps Resulting from Fiber Variation in the Canine Ventricles

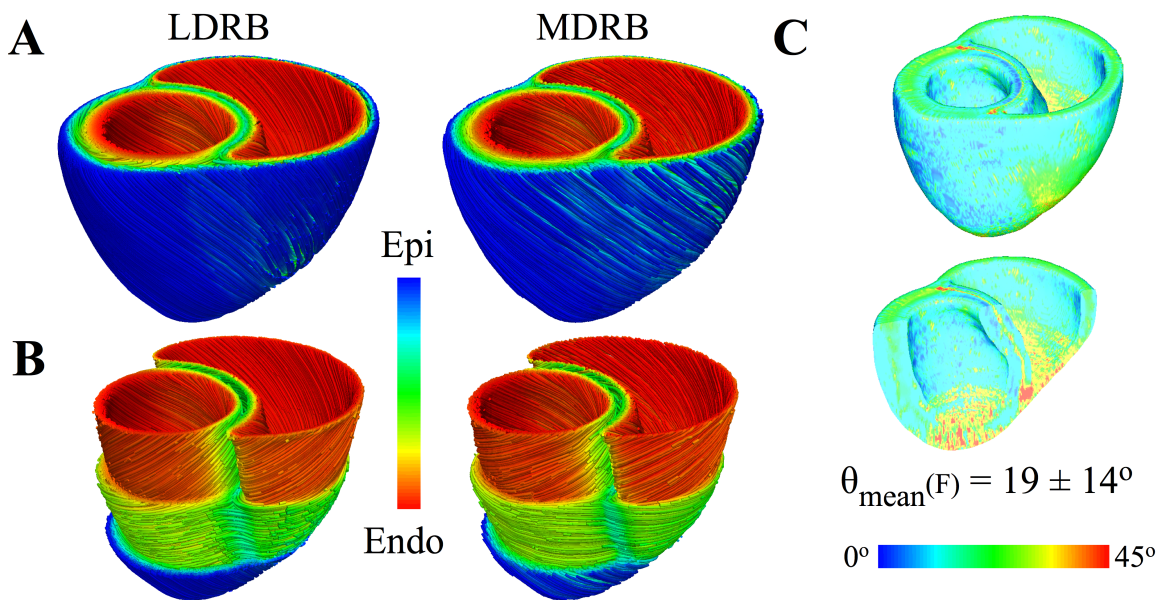
To understand how the values in Table 1 of the manuscript change when the LDRB inputs α and β are varied, the DTI-derived activation map was compared to activation maps calculated from the canine ventricles model with various LDRB fiber orientations. The α and β listed in the Results section “LDRB Fiber Orientation in the Model of the Canine Ventricles” of the manuscript were scaled in increments of 25% from 0 to 125%. The methods for the simulations, calculation of activation maps, and activation time statistics were identical to those described in the manuscript. The results are shown in S-Table 1.

S-Table 1: Activation time statistics for the model of the canine ventricles

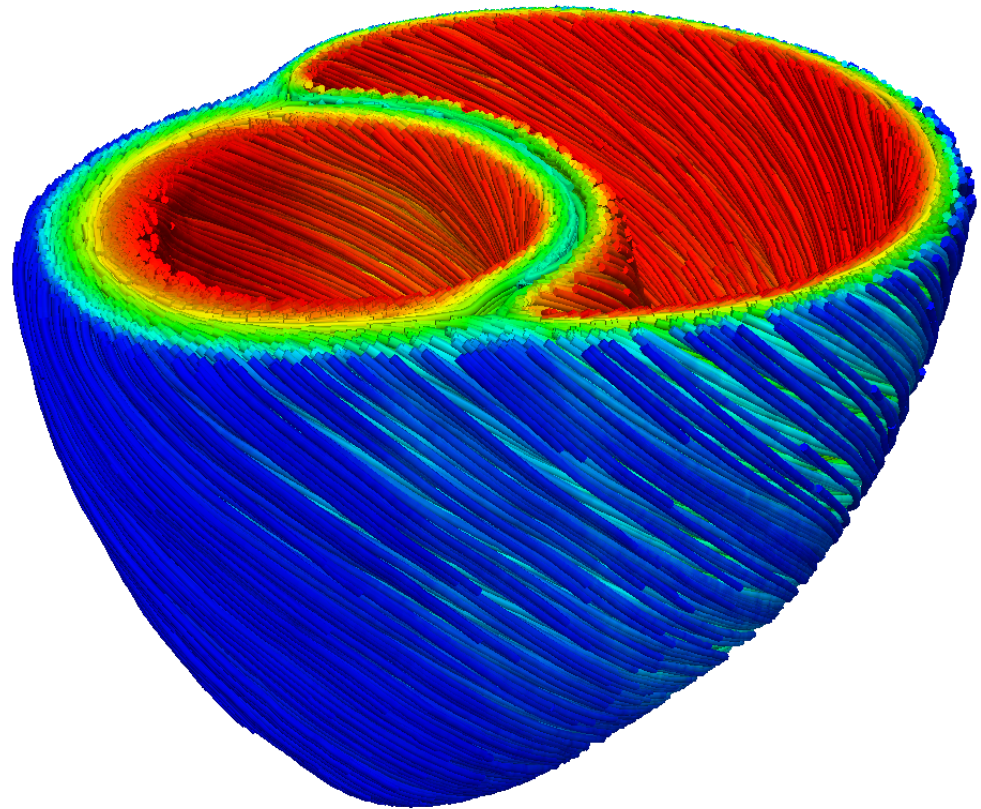
| | Activation Map Comparisons AT _{LDRB} vs. AT _{DTI} | |
|------------------------|---|----------------|
| | LV epi pacing | LV apex pacing |
| $\alpha, \beta * 0$ | | |
| RD (%) | 42 | 54 |
| RMSD (msec) | 14.13±18.65 | 25.85±21.10 |
| max. ΔAT (msec) | 70 | 67 |
| CC | 0.69 | 0.93 |
| $\alpha, \beta * 0.25$ | | |
| RD (%) | 22 | 38 |
| RMSD (msec) | 8.40±9.08 | 18.93±13.27 |
| max. ΔAT (msec) | 47 | 55 |
| CC | 0.88 | 0.96 |
| $\alpha, \beta * 0.50$ | | |
| RD (%) | 14 | 23 |
| RMSD (msec) | 5.42±5.61 | 11.96±7.71 |
| max. ΔAT (msec) | 33 | 32 |
| CC | 0.94 | 0.97 |
| $\alpha, \beta * 0.75$ | | |
| RD (%) | 9 | 12 |
| RMSD (msec) | 3.35±3.64 | 6.19±4.13 |
| max. ΔAT (msec) | 24 | 19 |
| CC | 0.97 | 0.98 |
| $\alpha, \beta * 1.00$ | | |
| RD (%) | 4 | 6 |
| RMSD (msec) | 1.48±1.42 | 3.15±2.28 |
| max. ΔAT (msec) | 8 | 11 |
| CC | 0.99 | 0.99 |
| $\alpha, \beta * 1.25$ | | |
| RD (%) | 7 | 8 |
| RMSD (msec) | 3.03±2.06 | 3.82±3.04 |
| max. ΔAT (msec) | 19 | 18 |
| CC | 0.98 | 0.98 |

4 Comparison of Laplace-Dirichlet and Minimal-Distance Rule-Based Fiber Orientations in the Canine Ventricles

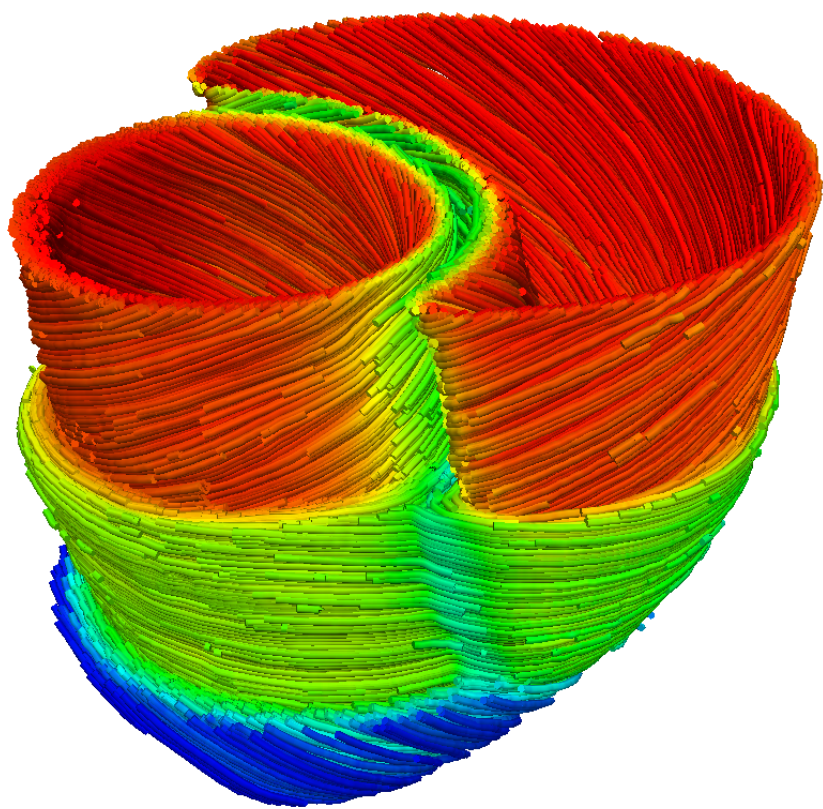
Results from the LDRB algorithm were compared to those from the minimal-distance rule-based (MDRB) method in Potse et al.² Since this MDRB algorithm only includes a rotation for the longitudinal fiber direction, we adjusted it to only match the α used by our LDRB algorithm for the canine ventricles ($\alpha_{endo} = 40^\circ$ and $\alpha_{epi} = -50^\circ$), and set the tissue conductivities of the model to 0.5 (S/m) along the longitudinal direction, and to 0.16 (S/m) for all directions perpendicular to the longitudinal direction. The results of these tests are shown in S-Figures 13-16 and in S-Table 2.



S-Figure 13: The LDRB and MDRB longitudinal fiber direction (F) in the model of the canine ventricles. (A) The streamlined LDRB and MDRB longitudinal fiber directions defined by the angle α . (B) Streamlines peeled away to visualize the internal longitudinal fiber directions. (C) The mean angle ($\theta_{mean}(F)$) between the LDRB and MDRB longitudinal fiber directions.



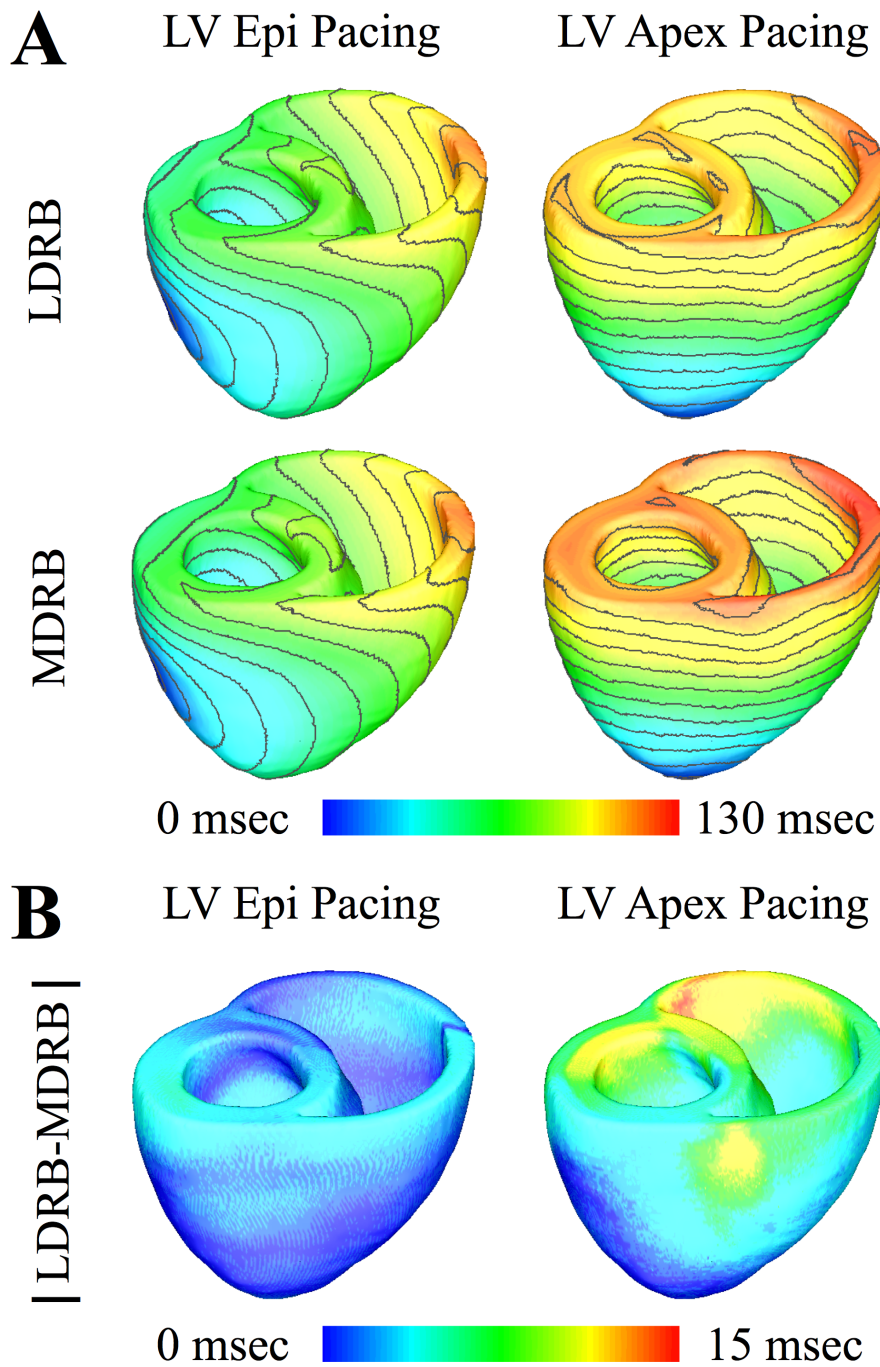
S-Figure 14: Streamlined MDRB F



S-Figure 15: Streamlined MDRB F

S-Table 2: Activation time statistics for the model of the canine ventricles

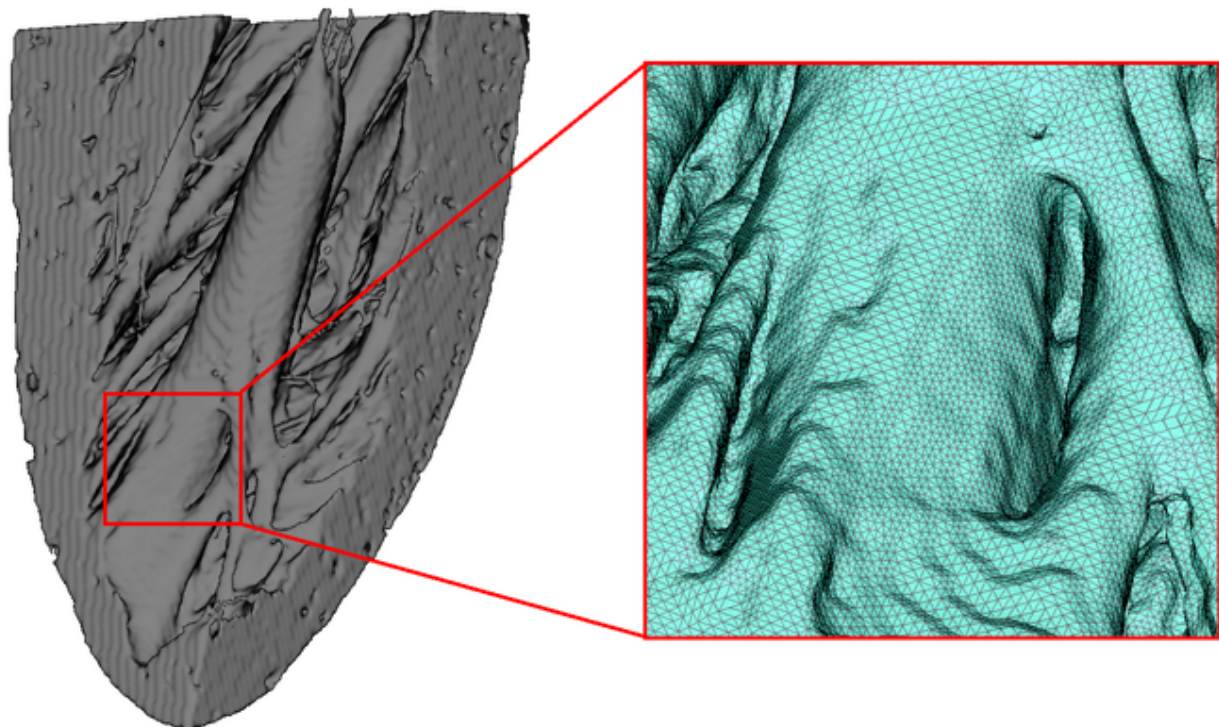
| Activation Map Comparisons AT_{LDRB} vs. AT_{MDRB} | | |
|--|-----------------|-----------------|
| | LV epi pacing | LV apex pacing |
| RD (%) | 3 | 7 |
| RMSD (msec) | 1.19 ± 1.04 | 4.15 ± 2.79 |
| max. $ \Delta AT $ (msec) | 7 | 16 |
| CC | 0.99 | 0.99 |



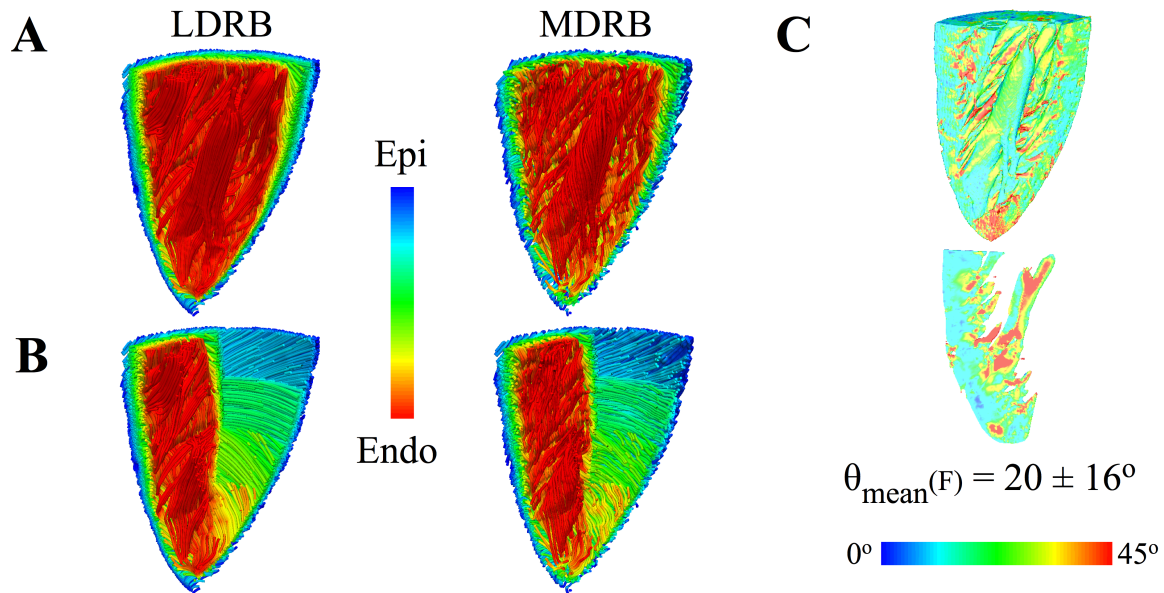
S-Figure 16: Simulation results from the model of the canine ventricles. (A) Activation maps obtained with the model of the canine ventricles with LDRB and MDRB fiber orientations during pacing at the LV epicardium and LV apex. Isochrone lines have a 10 ms spacing. (B) The absolute difference between the activation maps in (A).

5 High-Resolution Model of Rabbit Left Ventricle

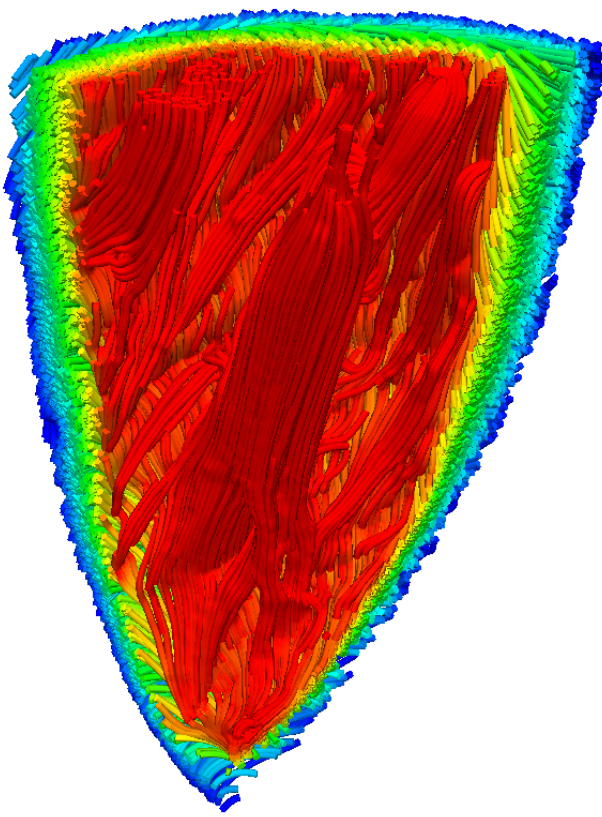
A high-resolution model of a rabbit LV wedge was constructed from high-field MRI data (isotropic voxel resolution of $\sim 25 \mu\text{m}$) collected from an adult rabbit heart at the University of Oxford.¹ The construction of the model was performed using the procedures outlined in the section “Development of a Model of the Canine Ventricles” in the manuscript. The mesh contained 7.1 million tetrahedra and 1.2 million nodes with an average edge length of $115 \mu\text{m}$. S-Figure 17 shows the mesh of the rabbit LV wedge with detailed endocardial structures. The LDRB was simplified to only compute $\nabla\phi_{lv}$ as the transmural direction in the model, and α_{endo} was set to 90° and α_{epi} to -60° . The MDRB algorithm described in Section 4 above was also applied to this model using these parameters. S-Figures 18-22 show the results from the LDRB and MDRB algorithms in this mesh. These results reveal that the LDRB algorithm, and not the MDRB algorithm, is capable of automatically incorporating continuous fiber orientation into complex endocardial structures according to rule R3 in the manuscript.



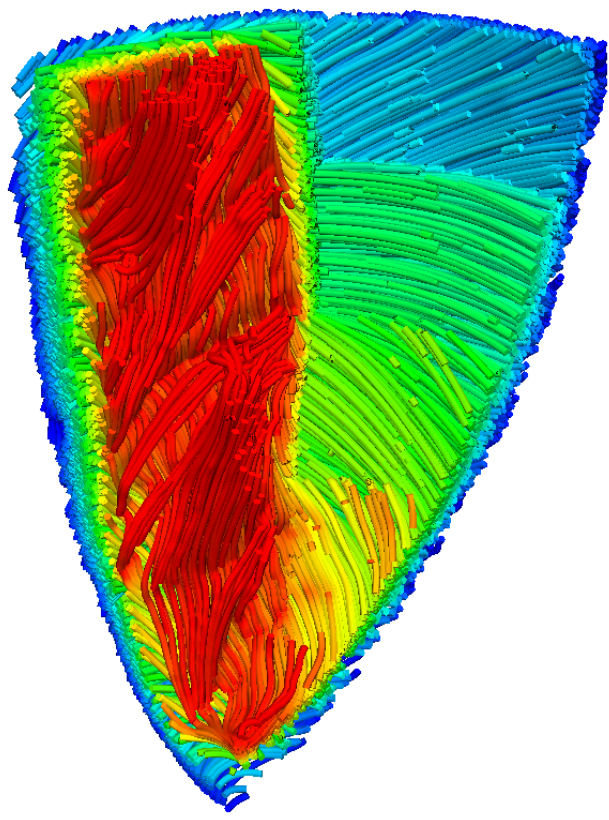
S-Figure 17: Computational mesh for the rabbit LV wedge model.



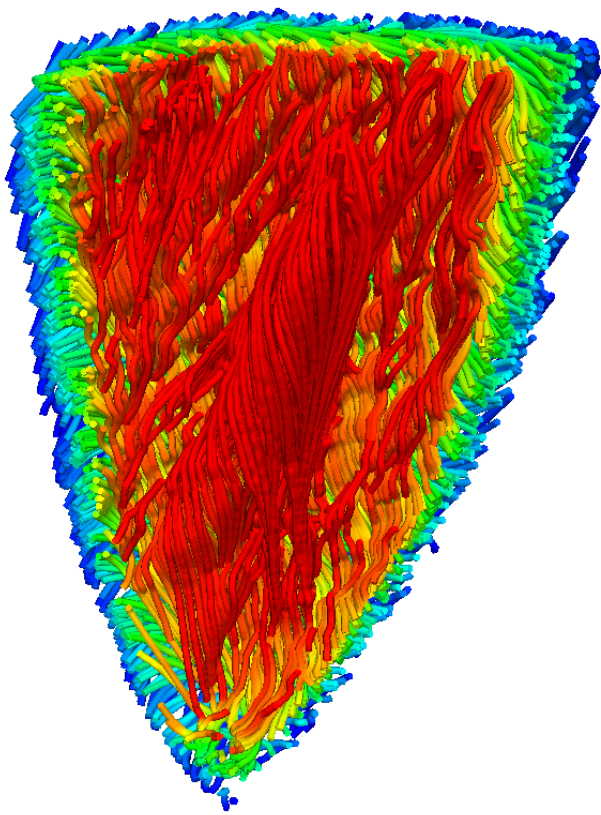
S-Figure 18: The LDRB and MDRB longitudinal fiber direction (F) in the model of the rabbit LV wedge model. (A) The streamlined LDRB and MDRB longitudinal fiber directions defined by the angle α . (B) Streamlines peeled away to visualize the internal longitudinal fiber directions. (C) The mean angle ($\theta_{\text{mean}}(F)$) between the LDRB and MDRB longitudinal fiber directions. The cross section in (C) was taken through the center of the papillary muscle.



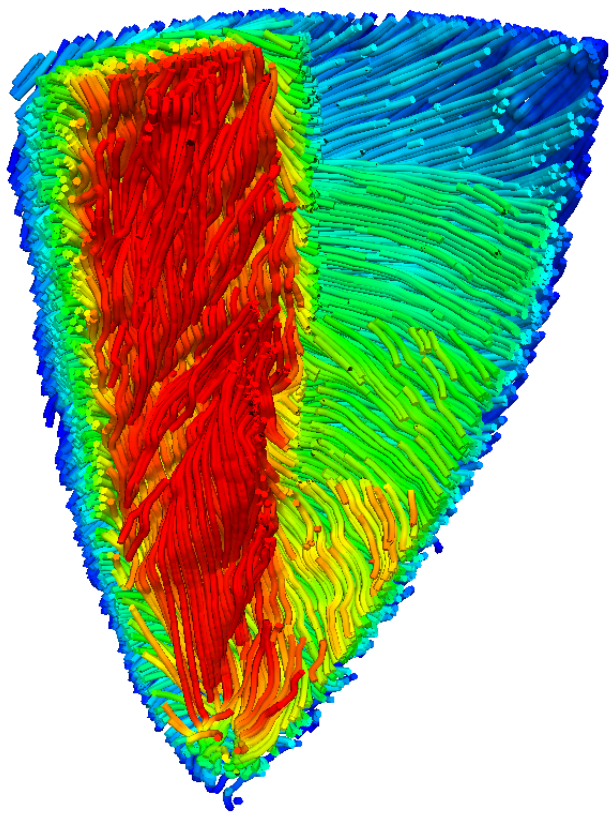
S-Figure 19: Streamlined LDRB F



S-Figure 20: Streamlined LDRB F



S-Figure 21: Streamlined MDRB F



S-Figure 22: Streamlined MDRB F

References

- [1] Burton, R.A., G. Plank, J.E. Schneider, V. Grau, H. Ahammer, S.L. Keeling, J. Lee, N.P. Smith, D. Gavaghan, N. Trayanova, and P. Kohl. Three-dimensional models of individual cardiac histoanatomy: tools and challenges. *Ann NY Acad Sci*, 1080:301-319, 2006.
- [2] Potse, M., B. Dub, J. Richer, A. Vinet, and R.M. Gulrajani. A comparison of monodomain and bidomain reaction-diffusion models for action potential propagation in the human heart. *IEEE Trans Biomed Eng*, 53(12 Pt 1):2425-2435, 2006.
- [3] Shoemake, K. Animating rotation with quaternion curves. *SIGGRAPH Comput. Graph.*, 19:245-254, 1985.